RSC Advances

PAPER

View Article Online
View Journal | View Issue

Check for updates

Cite this: *RSC Adv.*, 2022, **12**, 20523

Mechanism of the Fe(III)-catalyzed synthesis of hexahydropyrimidine with α-phenylstyrene: a DFT study†

Yaxuan Cheng, Siwei Yang, Chaoyu Zhao and Huiling Liu *

Received 29th April 2022
Accepted 1st July 2022

DOI: 10.1039/d2ra02727e

rsc.li/rsc-advances

It is very important to develop multiple C–H substitution reactions of simple alkenes to obtain complex unsaturated components. The present study focuses on a theoretical investigation of the plausible mechanism in the $\mathbf{Fe(OTf)_3}$-catalyzed tandem amidomethylative reactions of α-phenylstyrene. Bis(tosylamido)methane is activated by $\mathbf{Fe(OTf)_3}$ to form tosylformaldimine and its $\mathbf{Fe(OTf)_3}$-adduct. The $\mathbf{Fe(OTf)_3}$-adduct undergoes an intermolecular aza-Prins reaction with α-phenylstyrene to form allylamide. The DFT data support the formation of the hexahydropyrimidine derivative from allylamide, and "condensation/iminium homologation/intramolecular aza-Prins" is the optimal reaction path. At the same time, a possible reaction pathway for the conversion of the hydrolysate 1,3-diamide derivative to the hexahydropyrimidine (HHP) derivative is given. This work is thus instructive for understanding Fe(III)-based tandem catalysis for the amidomethylative multiple-substitution reactions of alkenes.

1. Introduction

Nitrogen heterocyclic compounds are widely found in nature and have good bioactivity and reactivity.[1–3] Among them, hexahydropyrimidines (HHPs) are promising compounds due to their important role in obtaining natural molecules, drugs and bioactive compounds.[4–8] Consequently, the search for more efficient synthesis approaches to obtain HHP and its derivatives has become a research hotspot.

In the past few years, researchers have developed a number of methods to synthesize HHPs with different substituted groups. Among them, the classical method utilizes the condensation of aldehydes or ketones with 1,3-diaminopropanes.[9–11] Based on this, Katritzky *et al.* prepared N,N′-unsymmetrically substituted HHPs through the cyclocondensation property of benzotriazole.[12] Subsequently, Khan *et al.* reported several novel 1,2,3-trisubstituted HHP derivatives, which were further prepared by the reaction of 1,3-diaminopropanes with different formaldehyde substitutes.[13] Due to the proposal of green chemistry, the concept of pursuing atom economy, process economy and environmental friendliness in chemical synthesis has been widely adopted.[14] Multicomponent reactions (MCRs) can meet the above requirements to a large extent.[15–19] In 2007, Liang *et al.* synthesized 1,3-diaryl-5-spirohexahydropyrimidines by a one-pot reaction using anilines, formaldehyde, and cyclohexanones.[20] In the same year, Farrell *et al.* synthesized novel phenol-derivatized HHPs by the Mannich reaction.[21] Meanwhile, Mukhopadhyay and colleagues synthesized 1,3-diaryl-HHPs catalysed by $FeCl_3$ in DCM in a one-pot reaction through the multicomponent approach using 1,3-dicarbonyl compounds, amines and formaldehyde.[22] In 2012, $\mathbf{In(OTf)_3}$ as a reusable Lewis acid catalyst for the synthesis of spiro-HHP scaffolds was first reported. This is a three-component system consisting of aromatic amines, formaldehyde, and cyclic ketones as substrates.[23] Although the above studies on the synthesis of HHPs have their own merits, they mainly focus on the reaction of C═O bonds and primary amines. In 2017, Cui *et al.* investigated the acid-catalyzed [2 + 2 + 2] system for HHPs, which overcame the challenge of insufficient nucleophilicity of the iminium species using the intermolecular aza-Prins reaction[24–27] and directly synthesizing the target product from the alkene precursor.[28] On the basis of this mechanism detection experiment, Fang *et al.* calculated the possible reaction mechanisms, catalytic species, and regioselectivity in the cycloaddition reaction for this system using density functional theory.[29] These studies provide a good theoretical basis for the tandem reaction and new ideas for the synthesis of HHP and its derivatives.

Recently, inspired by the above [2 + 2 + 2] tandem cycloaddition reaction[30–34] catalytic pathway, Cui *et al.* reported a tandem amidomethylative reaction catalyzed by Fe(III).[35] When multiple amidomethylation steps occurred through the elimination of the recovered C═C bonds, HHPs were directly

---

Laboratory of Theoretical and Computational Chemistry, Institute of Theoretical Chemistry, College of Chemistry, Jilin University, Liutiao Road 2, Changchun 130023, China. E-mail: huiling@jlu.edu.cn

† Electronic supplementary information (ESI) available. See **https://doi.org/10.1039/d2ra02727e**

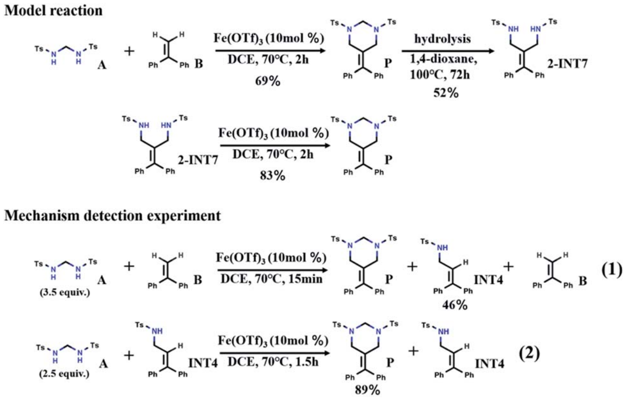

Scheme 1 The Cui *et al.* proposed model reaction and mechanism detection experiment.

synthesized from α-substituted styrene derivatives. As shown in Scheme 1, the yield of HHP (**P**) from the reaction of bis(tosylamido)methane (**A**) and α-phenylstyrene (**B**) is 69% (DCE = 1,2-dichloroethane, 70 °C, 2 h). Under hydrolysis conditions, **P** can form 52% 1,3-diamide derivative (**2-INT7)** (1,4-dioxane, 100 °C, 72 h). Interestingly, **2-INT7** can also generate **P** in 83% yield (DCE, 70 °C, 2 h). To understand the reaction mechanism, Cui *et al.* further performed probing experiments. After reacting for 15 min, the reaction of **A** and **B** was interrupted to generate the allylamide (**INT4**) with a yield of 46%. **A** continued to react with **INT4** for 1.5 hours to obtain **P** with a yield of 89%. Based on the above analysis of the experimental results, we speculate that there may be another path (**A** + **B** → **INT4** → **2-INT7** → **P**), which has aroused our interest in its further exploration. Here, we hope to find supportive reaction pathways through DFT computation and investigate some details of the catalytic mechanism at the molecular level, which will help us gain insight into the reaction mechanism of the tandem amidomethylation of alkenes.

2. Computational methods

In the present study, we used **Fe(OTf)$_3$** as the catalyst and bis(-tosylamido)methane (**A**) and α-phenylstyrene (**B**) as reactants for the model reaction. All geometries were fully optimized at the B3LYP-D3(BJ)/BSI level.[29,36–38] BSI denotes the SDD[39] pseudopotential for Fe and the 6-31G(d,p) basis set for all nonmetal atoms. Intrinsic reaction coordinate (IRC)[40,41] calculations were carried out to verify the transition structures connecting the substrates and products. The single-point energies of the reactants, transition states, intermediates and products in the two potential reaction paths were calculated. Single-point energy calculations were performed on the stationary points using the SMD model[42] and DCE (1,2-dichloroethane, $\varepsilon = 10.1$)/BSII level (the basis set of SDD for Fe and 6-311++G(d,p) for nonmetal atoms). All calculations were performed using the Gaussian 09 D.01 package.[43] Molecular structures were visualized using CYLview.[44] Contents related to the electronic structures were analyzed by Multiwfn.[45,46]

3. Results and discussion

Based on the report by Cui *et al.*, we propose two potential pathways for the model reaction (Fig. 1). The first step describes the generation of tosylformaldimine (**R2**) and its **Fe(OTf)3**-adduct (**R1**). Subsequently, the intermolecular reaction (aza-Prins) between **R1** and α-phenylstyrene (**B**) to form allylamide (**INT4**) occurs.

In order to explore the reaction mechanisms, we first performed an electrostatic potential analysis (ESP)[47] on **INT4** (Fig. 2a) to determine the possible reaction sites and further predict the potential reaction pathways. The ESP results show that above the carbon–carbon double bond and the nitrogen atom, there are regions with a negative electrostatic potential, which can easily be attacked by electrophiles. At the same time, due to the influence of the oxygen atom's solitary nature on electrons, there is an intersecting area above the nitrogen and oxygen atoms, which makes the electrostatic potential value (-17.34 kcal mol^{-1}) here smaller than that above the carbon–carbon (-8.25 kcal mol^{-1}) double bond. Through the ESP analysis above, it is seen that N_1 and C_2 are both nucleophilic and easily attacked by electrophiles. However, the optimal reaction site has not yet been determined. Therefore, we further used natural population analysis (NPA) to determine the optimal reaction site (Fig. 2b). According to the NPA charge analysis of **INT4**, the N_1 atom has a more negative charge value (-0.867) than the C_2 (-0.165) atom, which clearly shows that N_1 is more vulnerable to electrophilic attack and is the optimal reaction site in **INT4**.

At this point, **R1** has two competitive options: pathway 1, where **R1** attacks the N_1 atom in **INT4**, and pathway 2, where **R1** attacks the C_2 atom on the double bond in **INT4**. We have determined the optimal pathway through DFT calculations, and the specific analysis will be introduced in the following subsections.

3.1 Tosylformaldimine release reaction

Bis(tosylamido)methane (**A**) is readily synthesized under alkaline conditions and can be activated by Lewis acids to form formaldimine. In this process, the main role of **Fe(OTf)$_3$** is to promote the activation of bis(tosylamido)methane to form tosylformaldimine. Based on a previous [2 + 2 + 2] cyclic addition mechanism study,[48] an intermolecular aza-Prins process should be followed in this reaction, which requires the catalyst to react with **A** first to release **R2**. The free energy profile for the whole tosylformaldimine release reaction process is shown in Fig. 3a, where the total free energy of **A** and **Fe(OTf)$_3$** is set to the reference energy. Since the N atom in **A** has a lone electron pair and can coordinate with the catalyst, the catalyst **Fe(OTf)$_3$** combines with **A** to produce the intermediate **INT1**, in which the negative charge is focussed on the Fe site and the positive charge is focussed on the adjacent N atom. Then, the intermediate **INT1** undergoes a process involving C–N bond breaking along with hydrogen transfer to generate **R1**. This process needs to overcome an energy barrier of 31.1 kcal mol^{-1}, and the reaction free energy is 1.2 kcal mol^{-1}. Meanwhile, we

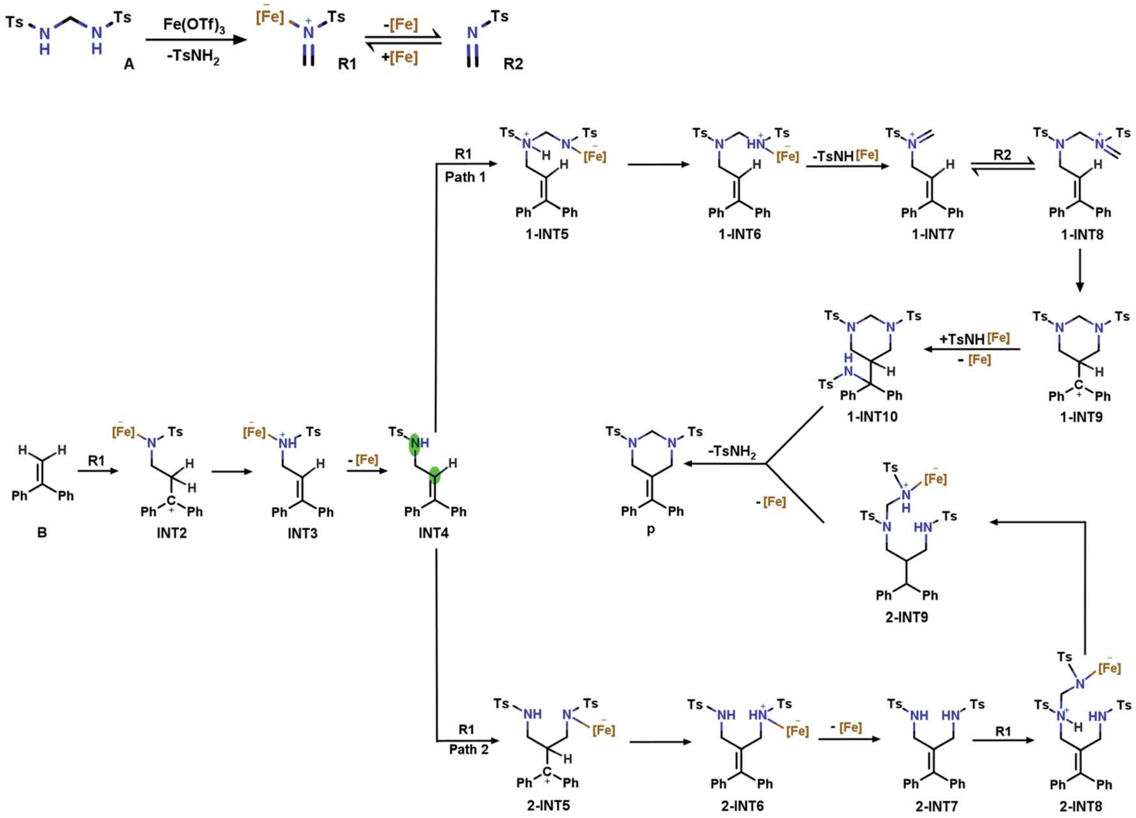

Fig. 1 Two plausible tandem catalytic pathways with α-phenylstyrene.

also tried to use **A** as a base to deliver protons, but the protons to be delivered are encased inside the molecule **INT1** (Fig. S1†), and due to steric hindrance, there was no place for **A** to form a six-membered ring transition state. Therefore, using **A** as a base for delivering protons was not successful. Eventually, **Fe(OTf)$_3$** departed from **R1** to generate **R2**, with a reaction free energy of 18.0 kcal mol^{-1}. From Fig. 3a, we can observe that the rate-determining step of **R2** being released from **A** is a hydrogen transfer process, which has a relatively high energy barrier and requires a certain temperature for the reaction to occur.

3.2 Intermolecular aza-Prins reaction

After **R1** is released from **A** in the previous step, the nucleophile **B** attacks the atom C$_1$ in **R1**, completing the intermolecular aza-Prins reaction. The free energy profile for the whole intermolecular aza-Prins reaction process is shown in Fig. 3b, where the total free energy of **B** and **R1** is set to the reference energy. The complexation of **R1** and **B** undergoes nucleophilic addition *via* a transition state **TS2** with a low energy barrier of 1.9 kcal mol^{-1}, which indicates that the process is extremely easy to proceed. Subsequently, the atom N$_1$ in **INT2** undergoes protonation and a hydrogen is transferred from the C$_2$ to N$_1$, which needs to overcome an energy barrier of 34.0 kcal mol^{-1}. In Cui's experiments, the HHP (**P**) yield was low (less than 70%) and was not improved by increasing the reaction temperature (70 °C/90 °C/110 °C). Our calculation results show that the energy difference between the initial state **INT2** and the final state **INT3** is very small (only 1.4 kcal mol^{-1}), which indicates that the yield will not increase with the increase in temperature, and so the activation energy barrier of 34.0 kcal mol^{-1} required from the initial state **INT2** and the final state **INT3** is feasible. As shown in Fig. S1,† the distance of the nitrogen–hydrogen bond is shortened from 2.805 Å in **INT2** to 1.433 Å in **TS3**. This indicates that higher energy barriers need to be crossed at the hydrogen transfer stage. The distance from C$_2$ to H$_2$ in **TS3** is 1.363 Å. Finally, C=C is formed in **INT4** as the catalyst **Fe(OTf)$_3$** leaves from **INT3**.

3.3 Catalytic pathways begin with condensation and aza-Prins

B undergoes an intermolecular aza-Prins reaction to form **INT4**. In the subsequent tandem step of **INT4**, **R1** has two competing options in the subsequent tandem steps: a condensation reaction or another aza-Prins reaction. Experimentally, it is difficult to compare these two competing behaviours. Here, we calculated the energies of the reactants, products and transition states, and analyzed them according to their activation energy. In the following sections, the elemental steps for the two competing pathways will be discussed in detail.

3.3.1 Pathway 1 begins with the condensation reaction

The first part of the condensation reaction. The free energy profile for the whole condensation reaction process is shown in Fig. 4a, where the total free energy of **INT4** and **R1** is set to the reference energy. **INT4** forms **1-INT5** on its N-center with **R1**,

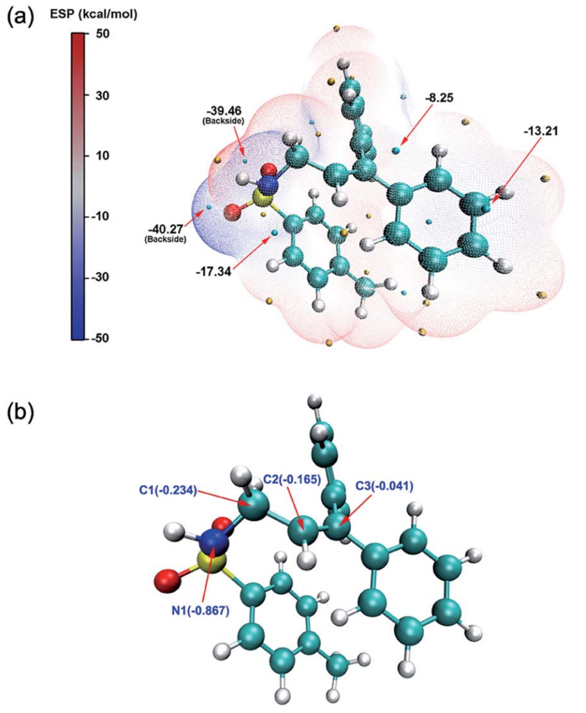

Fig. 2 (a) ESP (electrostatic potential) distribution on the van der Waals surface of the **INT4** molecule. The salient surface local minima and maxima of ESP are represented by cyan and orange spheres, respectively, and the local minima point values are marked with dark black text. The unit is kcal mol^{-1} (b) NPA (natural population analysis) of the **INT4** molecule. The NPA charge value of the main atom is marked in blue text. The yellow, red, cyan and white spheres represent sulfur atoms, oxygen atoms, carbon atoms, and hydrogen atoms, respectively.

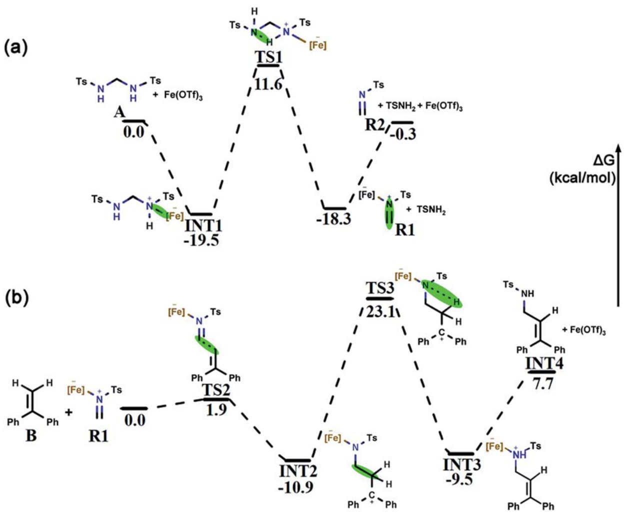

Fig. 3 (a) Free energy profile for the tosylformaldimine release reaction. (b) Free energy profile for the intermolecular aza-Prins reaction. The green mark in the figure is the reaction area. The relative Gibbs free energies are show in kcal mol^{-1}.

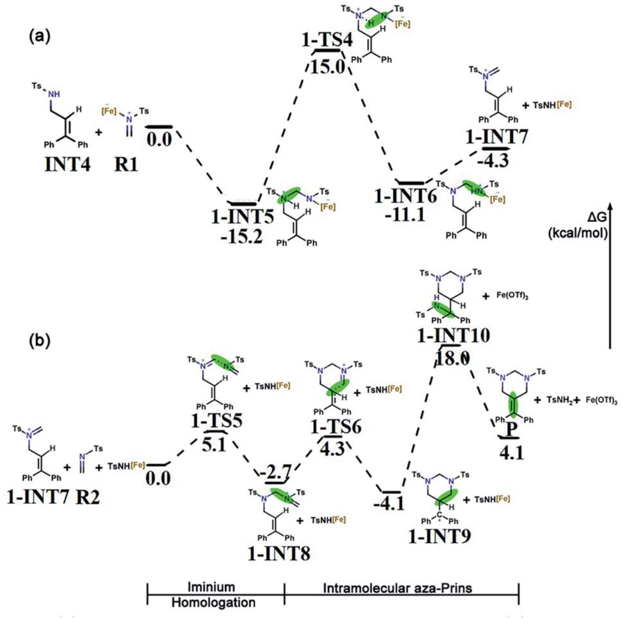

Fig. 4 (a) Free energy profile for the condensation reaction. (b) Free energy profile for the iminium homologation and intramolecular aza-Prins reaction. The green regions in the figure denote the reaction area. The relative Gibbs free energies are given in kcal mol^{-1}.

and no transition state is found in this process. The free energy of **1-INT5** is 15.2 kcal mol^{-1} lower than that of the reactant (**INT4** + **R1**), indicating that this step is favored thermodynamically. Subsequently, the hydrogen atom on the N_1 atom in **1-INT5** is transferred to the N_2 atom to form **1-INT6**. This hydrogen transfer step requires overcoming an energy barrier of 30.2 kcal mol^{-1}. The broken N_1–H_3 bond distance increases from 1.029 Å in **1-INT5** to 2.450 Å in **1-INT6** and the formed N_2–H_3 bond shortens from 2.528 Å in **1-INT5** to 1.033 Å in **1-INT6** (Fig. S1†). The next step is the departure of **TsNH[Fe]** to provide **1-INT7**. Although this step is an endergonic process, the free energy difference between the reactant and product is only 6.8 kcal mol^{-1}, which means that this stage is still feasible. In addition, the bond length between N_1 and C_4 in **1-INT7** is 1.274 Å (between N_1 and C_4 in **1-INT6** is 1.425 Å), which indicates that after **TsNH[Fe]** is separated, a double bond is formed between carbon and nitrogen.

Iminium homologation. In the second part of the tandem path 1, the iminium homologation reaction occurs. **R2** attacks the C_4 in **1-INT7** and the C_4=N_1 bond (1.274 Å) breaks to form the C_4–N_1 bond (1.500 Å) through the transition state **1-TS5** to produce **1-INT7**'s iminium homolog **1-INT8**. As shown in Fig. S1,† the distance between N_3 and C_4 in the transition state **1-TS5** is 2.001 Å. Here, a single bond is formed. The energy barrier to be overcome is 5.1 kcal mol^{-1} and the energy difference between the reactant and product is only 2.7 kcal mol^{-1}, indicating that this is a reversible process and the conversion between the two intermediates is very easy to achieve.

Intramolecular aza-Prins reaction. In the last part, an intramolecular aza-Prins reaction occurs in the intermediate **1-INT8**. In this process, the C_5 atom in **1-INT8** attacks the C_2

atom on styrene to form a closed six-membered ring, which only needs to overcome a low energy barrier of 7.0 kcal mol^{-1}. The distance between C_5 and C_2 is reduced from 3.300 Å to 1.595 Å (Fig. S1†). The difference in free energy between the reactant **1-INT8** and the product **1-INT9** is 1.4 kcal mol^{-1}, making this intramolecular aza-Prins reaction extremely easy to carry out. The **TsNH[Fe]** isolated from the condensation reaction attacks the carbocation in the intermediate **1-INT9**, the hydrogen atom is transferred and the carbocation is captured, and the product **P** is obtained. In this process, **1-INT10** is 22.1 kcal mol^{-1} higher than **1-INT9.** The free energy profile for the iminium homologation and intramolecular aza-Prins reaction process is shown in Fig. 4b, where the total free energy of **1-INT7**, **R2** and **TsNH[Fe]** is set to the reference energy.

3.3.2 Pathway 2 begins with the aza-Prins reaction

Intermolecular aza-Prins reaction. Similar to the formation of **INT4**, **R1** electrophilically attacks the C_2 atom in **INT4** to form **2-INT5**, and the intermolecular aza-Prins reaction occurs again. The free energy profile for the whole intermolecular aza-Prins reaction process is shown in Fig. 5a, where the total free energy of **INT4** and **R1** is set to the reference energy. This reaction has an exergonic free energy of −8.4 kcal mol^{-1}. Moreover, the energy barrier to be overcome in this process *via* the transition state **2-TS4** is only 1.0 kcal mol^{-1}. As shown in Fig. S2,† the distance between C_6 and N_4 increases from 1.277 Å in **R1** to 1.451 Å in **2-INT5**, and the double bond is broken to form a single bond. In addition, the hydrogen transfer in **2-INT5** overcomes an energy barrier of 45.4 kcal mol^{-1} to obtain the intermediate **2-INT6**, from which the catalyst **Fe(OTf)$_3$** is separated. The rate-determining step of this stage is the hydrogen transfer process, which is kinetically unfavorable as it needs to cross an energy barrier of 45.4 kcal mol^{-1}.

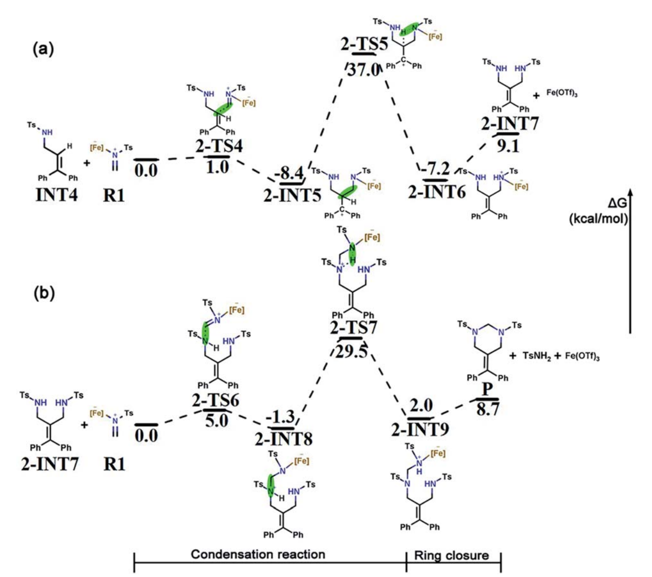

Fig. 5 (a) Free energy profile for the intermolecular aza-Prins reaction. (b) Free energy profile for the condensation and six-membered ring closure. The relative Gibbs free energies are given in kcal mol^{-1}.

Condensation reaction. The goal in this part is to introduce a carbon atom on **2-INT7**, which is achieved using the condensation between **R1** and **2-INT7**. The condensation of **2-INT7** and **R1** only has a 5.0 kcal mol^{-1} energy barrier to overcome, and the difference in free energy between the products and the reactants is very small. As shown in Fig. S2,† the distance between C_7 and N_4 is 1.556 Å in **2-INT8**, and this condensation reaction forms a single bond. Nevertheless, the energy barrier (30.8 kcal mol^{-1}) to overcome for hydrogen transfer after the formation of intermediate **2-INT8** is relatively high. Therefore, the reaction requires a high temperature and a long time.

Six-membered ring closure. The C_7 in **2-INT9** is connected to N_1 to achieve a six-membered ring closure reaction. There is no transition state in the above process. The catalyst **Fe(OTf)$_3$** and **TsNH$_2$** are separated, and the target product **P** is obtained by the direct ring closure of **2-INT9**. The energy difference between the reactant and product is only 6.7 kcal mol^{-1}, indicating that this process is easy to implement. The free energy profile for the condensation reaction and the six-membered ring closure process is shown in Fig. 5b, where the total free energy of **2-INT7** and **R1** is set to the reference energy.

In summary, the results compared through theoretical calculations show that pathway 1, starting with a condensation reaction, is preferable to pathway 2, starting with the aza-Prins reaction because the **INT4** + **R1** → **1-INT5** stage in pathway 1 has a greater exergonic free energy (6.8 kcal mol^{-1}) than the **INT4** + **R1** → **2-INT5** stage in pathway 2. Moreover, the Laplacian bond order (LBO) is a parameter that can measure the bond strength in organic systems. We calculated the LBO for the N–H bond in **1-INT5** and the C–H bond in **2-INT5**, and obtained the values 0.79 and 0.87 (Fig. 6), respectively. This means that the cleavage of the C–H bond in the **2-INT5** → **2-INT6** process requires a higher energy than the cleavage of the N–H bond in the **1-INT5** → **1-INT6** process. Thus, the **2-INT5** → **2-INT6** stage in pathway 2 has a higher reaction energy barrier (15.2 kcal mol^{-1}) than the **1-INT5** → **1-INT6** stage in pathway 1. Therefore, the N_1 site serves as the optimal reaction site for **INT4** and has nucleophilicity. Pathway 1, starting with the condensation reaction, is thus the preferred mechanism. **A** and **B** react to form **P.** The

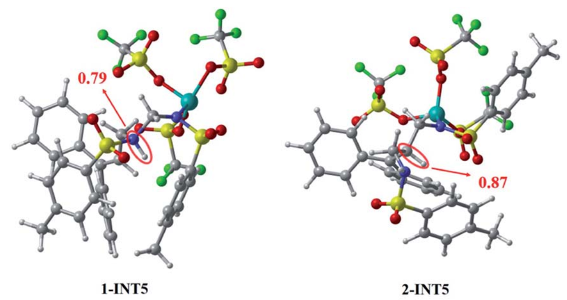

Fig. 6 The LBO of the molecules. The yellow, cyan, green, purple, red, gray and white spheres represent sulfur atoms, iron atoms, fluorine atoms, nitrogen atoms, oxygen atoms, carbon atoms, and hydrogen atoms, respectively.

hydrolysis product **2-INT7** can also form **P**, which is consistent with Cui's experimental results.

4. Conclusions

In this work, the calculation details of the mechanism of the reaction between bis(tosylamido)methane (**A**) with α-phenylstyrene (**B**) catalyzed by **Fe(OTf)$_3$** are clarified based on density functional theory. The analysis of electrostatic potential shows that the two reaction sites N_1 and C_2 in allylamide (**INT4**) are both nucleophilic, leading to two competing reaction pathways. Further, according to NPA charge analysis, the N_1 site shows more negative charge, is more vulnerable to **R1** electrophilic attack, and is the optimal site for the reaction. Through the reaction energy barriers of each step for the two competing reaction pathways, and the analysis and comparison of the reaction energy, it has been determined that pathway 1 is the preferred mechanism. The preferred catalyzed mechanism consists of five parts: (1) tosylformaldimine (**R2**) and its **Fe(OTf)$_3$**-adduct (**R1**) are released from **A**; (2) an intermolecular aza-Prins reaction produces **INT4**; (3) a condensation reaction to form **1-INT7**; (4) iminium homologation to form **1-INT8**; (5) an intramolecular reaction to form HHP (**P**). In this tandem reaction, **A** and **B** generate **P** *via* the intermediate **INT4**. Additionally, we found that the hydrolysis product 1,3-diamide derivative (**2-INT7**) can also undergo a condensation and ring closure reaction to generate **P**.

Conflicts of interest

There are no conflicts to declare.

References

1 A. Dhakshinamoorthy and H. Garcia, *Chem. Soc. Rev.*, 2014, **43**, 5750–5765.
2 M. Zhang, Q. Wang, Y. Peng, Z. Chen, C. Wan, J. Chen, Y. Zhao, R. Zhang and A. Q. Zhang, *Chem. Commun.*, 2019, **55**, 13048–13065.
3 P. C. Sharma, K. K. Bansal, A. Sharma, D. Sharma and A. Deep, *Eur. J. Med. Chem.*, 2020, **188**, 112016.
4 T. Gossas, H. Nordström, M.-H. Xu, Z.-H. Sun, G.-Q. Lin, H. Wallberg and U. H. Danielson, *Med. Chem. Commun.*, 2013, **4**, 432–442.
5 Y. Ochi, S. Yokoshima and T. Fukuyama, *Org. Lett.*, 2016, **18**, 1494–1496.
6 B. M. Williams and D. Trauner, *Angew. Chem., Int. Ed.*, 2016, **55**, 2191–2194.
7 T. Kang, S. Gao, L. X. Zhao, Y. Zhai, F. Ye and Y. Fu, *J. Agric. Food Chem.*, 2021, **69**, 45–54.
8 R. W. Sabnis, *ACS Med. Chem. Lett.*, 2021, **12**, 679–680.
9 R. F. Evans, *Aust. J. Chem.*, 1967, **20**, 1643–1661.
10 D. J. Bergmann, E. M. Campi, W. R. Jackson, Q. J. Mccubbin and A. F. Patti, *Tetrahedron*, 1997, **53**, 17449–17460.
11 J. M. Locke, R. Griffith, T. D. Bailey and R. L. Crumbie, *Tetrahedron*, 2009, **65**, 10685–10692.
12 A. R. Katritzky, S. K. Singh and H. Y. He, *J. Org. Chem.*, 2002, **67**, 3115–3117.
13 M. S. Y. KHAN and M. GUPTA, *Pharmazie*, 2002, **57**, 377–383.
14 R. C. Cioc, E. Ruijter and R. V. A. Orru, *Green Chem.*, 2014, **16**, 2958–2975.
15 E. Ruijter, R. Scheffelaar and R. V. Orru, *Angew. Chem., Int. Ed.*, 2011, **50**, 6234–6246.
16 A. Bhunia, S. R. Yetra and A. T. Biju, *Chem. Soc. Rev.*, 2012, **41**, 3140–3152.
17 C. de Graaff, E. Ruijter and R. V. A. Orru, *Chem. Soc. Rev.*, 2012, **41**, 3969–4009.
18 N. Deibl and R. Kempe, *Angew. Chem., Int. Ed.*, 2017, **56**, 1663–1666.
19 J. S. Zhang, L. Liu, T. Chen and L. B. Han, *Chem.–Asian J.*, 2018, **13**, 2277–2291.
20 H. L. Wei, Z. Y. Yan, Y. N. Niu, G. Q. Li and Y. M. Liang, *J. Org. Chem.*, 2007, **72**, 8600–8603.
21 J. R. Farrell, J. Niconchuk, C. S. Higham and B. W. Bergeron, *Tetrahedron Lett.*, 2007, **48**, 8034–8036.
22 C. Mukhopadhyay, S. Rana and R. J. Butcher, *Tetrahedron Lett.*, 2011, **52**, 4153–4157.
23 A. Dandia, A. K. Jain and S. Sharma, *Tetrahedron Lett.*, 2012, **53**, 5270–5274.
24 D. M. Kaphan, F. D. Toste, R. G. Bergman and K. N. Raymond, *J. Am. Chem. Soc.*, 2015, **137**, 9202–9205.
25 D. H. Ma, Z. L. Zhong, Z. M. Liu, M. J. Zhang, S. Y. Xu, D. Y. Xu, D. P. Song, X. G. Xie and X. G. She, *Org. Lett.*, 2016, **18**, 4328–4331.
26 J. F. Bai, K. Yasumoto, T. Kano and K. Maruoka, *Chem. – Eur. J.*, 2018, **24**, 10320–10323.
27 X. Y. Liu, F. P. Wang and Y. Qin, *Acc. Chem. Res.*, 2021, **54**, 22–34.
28 H. Zhou, H. Handi, C. Lakmal, J. M. Baine, H. U. Valle, X. Xu and X. Cui, *Chem. Sci.*, 2017, **8**, 6520–6524.
29 R. Fang, Y. C. Zhang, A. M. Kirillov and L. Z. Yang, *J. Org. Chem.*, 2020, **85**, 3676–3688.
30 G. Dominguez and J. Perez-Castells, *Chem. Soc. Rev.*, 2011, **40**, 3430–3444.
31 A. Roglans, A. Pla-Quintana and M. Sola, *Chem. Rev.*, 2021, **121**, 1894–1979.
32 W. K. Samba, R. Tia and E. Adei, *J. Phys. Org. Chem.*, 2021, **35**, 1.
33 C. S. Wang, Q. Sun, F. Garcia, C. Wang and N. Yoshikai, *Angew. Chem., Int. Ed.*, 2021, **60**, 9627–9634.
34 T. Yasui, R. Tatsumi and Y. Yamamoto, *ACS Catal.*, 2021, **11**, 9479–9484.
35 X. L. Qian, H. Zhou, H. H. C. Lakmal, J. Lucore, X. S. Wang, H. U. Valle, B. Donnadieu, X. Xu and X. Cui, *ACS Catal.*, 2020, **10**, 10627–10636.
36 A. D. Becke, *J. Chem. Phys.*, 1993, **98**, 5648–5652.
37 X. Zhang and K. Wang, *RSC Adv.*, 2015, **5**, 34439–34446.
38 A. R. Firooz, M. Movahedi and H. Sabzyan, *Mater. Sci. Eng., C*, 2019, **94**, 410–416.
39 D. Andrae, U. H. U. Ermann, M. Dolg, H. Stoll and H. Preu, *Theor. Chim. Acta*, 1990, **77**, 123–141.
40 K. Fukui, *J. Phys. Chem.*, 1970, **74**, 4161–4163.
41 K. Fukui, *Acc. Chem. Res.*, 1981, **14**, 363–368.

42 A. V. Marenich, C. J. Cramer and D. G. Truhlar, *J. Phys. Chem. B*, 2009, **113**, 6378–6396.

43 M. J. Frisch, G. W. Trucks, H. B. Schlegel, G. E. Scuseria, M. A. Robb, J. R. Cheeseman, G. Scalmani, V. Barone, B. Mennucci, G. A. Petersson, H. Nakatsuji, M. Caricato, X. Li, H. P. Hratchian, A. F. Izmaylov, J. Bloino, G. Zheng, J. L. Sonnenberg, M. Hada, M. Ehara, K. Toyota, R. Fukuda, J. Hasegawa, M. Ishida, T. Nakajima, Y. Honda, O. Kitao, H. Nakai, T. Vreven, J. A. Montgomery Jr., J. E. Peralta, F. Ogliaro, M. Bearpark, J. J. Heyd, E. Brothers, K. N. Kudin, V. N. Staroverov, T. Keith, R. Kobayashi, J. Normand, K. Raghavachari, A. Rendell, J. C. Burant, S. S. Iyengar, J. Tomasi, M. Cossi, N. Rega, J. M. Millam, M. Klene, J. E. Knox, J. B. Cross, V. Bakken, C. Adamo, J. Jaramillo, R. Gomperts, R. E. Stratmann, O. Yazyev, A. J. Austin, R. Cammi, C. Pomelli, J. W. Ochterski, R. L. Martin, K. Morokuma, V. G. Zakrzewski, G. A. Voth, P. Salvador, J. J. Dannenberg, S. Dapprich, A. D. Daniels, O. Farkas, J. B. Foresman, J. V. Ortiz, J. Cioslowski and D. J. Fox, *Gaussian 09, Revision D.01*, Gaussian Inc., Wallingford CT, 2013.

44 C. Y. Legault, *CYLview20*, Université De Sherbrooke, 2020.

45 T. Lu and F. Chen, *Acta Chim. Sin.*, 2011, **69**, 2393–2406.

46 T. Lu and F. Chen, *J. Comput. Chem.*, 2012, **33**, 580–592.

47 T. Lu and F. W. Chen, *J. Mol. Graphics Modell.*, 2012, **38**, 314–323.

48 Z. Y. Li, H. H. C. Lakmal and X. Cui, *Org. Lett.*, 2019, **21**, 3735–3740.